

SEMESTER THESIS

**Design and Optimization of Beam
Delivery for Readout and Doppler
Cooling of Trapped Ions**

Submitted by

Naman Gupta

as part of the Master's Degree in Quantum Engineering at ETH Zurich

Supervised by

DOMINIQUE ZEHNDER

TEREZA VISKOVA

DR. CORNELIUS HEMPEL

DR. JONATHAN HOME



ETH zürich

Ion Trap Quantum Computing (ITQC) Group,

Paul Scherrer Institute, Switzerland

Abstract

The need for scaling quantum computations to more number of ions has shifted the interest from using free space optics to integrated optical waveguides for light delivery to multiple ions. Achieving this requires precise control of laser beams and their delivery from their site of generation in a lab to the experimental setup. Doppler cooling and state readout of $^{40}Ca^+$ ions require the use of a precise controlled 397 nm laser. In this thesis, a closed-loop feedback based on an acousto-optic modulator (AOM) and a proportional-integral (PI) controller is implemented for power stabilization of the 397 nm laser. Additionally, addressing multiple ions at the same time necessitates the use of multiple laser beams. For near ultraviolet (UV) wavelengths, such as 397 *nm*, this is done through free space optical components assembled on a breadboard. In this semester project, the design and assembly of the setup for the delivery of the 397 nm laser beam to the experimental setup was done. This included stabilization of the power of the 397nm laser using a feedback loop, design and assembly of a 1-to-6 splitting board. The PI controller was realized with the SINARA Stabilizer, and a proportional gain $K_P = 14.125$ and an integrator crossover frequency of 60 *Hz* was found to stabilize the laser intensity to within 1%. As a result, a noise rejection bandwidth of 40 *kH**z* was achieved for the feedback loop, which was found to be limited by the latency of the SINARA stabilizer.

Acknowledgements

I would like to thank my supervisors Dominique Zehter and Tereza Viskova for their guidance throughout this project. I would also like to thank Julian Schmidt and Luška Milanovic for their extremely valuable inputs and direction. Additionally, I am grateful to the Ion Trap Quantum Computing group members for their welcoming attitude and support during my frequent visits to the laboratory.

Contents

Acknowledgements	ii
1 Introduction	1
2 The Acousto-Optic Modulator	5
2.1 Theory	5
2.2 The Single-pass Configuration	7
2.3 The Double-pass Configuration	8
3 Laser Intensity Stabilization	10
3.1 Fundamentals of Control Theory	10
3.1.1 The Proportional-Integral-Derivative (PID) Controller	14
3.2 Experimental Configuration	15
3.2.1 The Moku:Pro as a PID	15
3.2.2 The SINARA Stabilizer as a PID	18
3.3 Noise Rejection Bandwidth	22
4 The Splitting Board	26
4.1 Design	26
4.2 Hardware Considerations During Assembly	26
5 Conclusion	30
Bibliography	32

Chapter 1

Introduction

An ion trap quantum information system operates by trapping atomic ions and coherently controlling them to enable high-fidelity gate operations. This includes confining ions with DC and radio frequency (rf) electric fields to create a three-dimensional pseudoharmonic potential. Computational states are encoded in the atomic states of the ions as well as in the motional modes of the ion chain, making the system highly susceptible to destructive effects arising from heating and mechanical vibrations. Additionally, cooling and coherent manipulation of the quantum states of the ions requires addressing the ions with lasers. A well-known implementation is the surface electrode ion trap [1]. However, this involves laser beams that travel through several centimeters of free space before reaching the trap chip inside the vacuum chamber, making the laser beams vulnerable to mechanical drifts and beam-pointing instability, posing challenges for scalability [2].

Recent advances in scaling trapped ion platforms have shifted focus from free-space optical addressing of ions to on-chip integrated waveguide optical addressing within the surface-electrode ion trap chip [3, 4, 5]. In this approach, laser light is delivered via waveguide couplers fabricated just below the substrate that hosts the confining surface electrodes [5].

In the Ion Trap Quantum Computing group at the Paul Scherrer Institute, Calcium-40 ($^{40}Ca^+$) ions are used at cryogenic temperatures with an integrated optical waveguide trap chip similar to the one described above. The 397 nm laser is used for Doppler cooling and readout of calcium-40 ions in trapped ion experiments [6]. Laser light is delivered from the laser head to the experiment in the lab via polarization maintaining fibers. Laser power reaching the ions is susceptible to change over time as a result of drifts in the polarization of light at the output of polarization maintaining fibers, use of polarization sensitive optics, temperature fluctuations, and mechanical disturbances. Spurious reflections of the readout

laser (397 nm) from surfaces within the experimental setup give rise to dark counts. This is corrected by turning the repumper 866 nm ON and OFF. When the repumper is turned OFF, the electron remains in the $3^2D_{3/2}$ dark state, and therefore the observed counts are due solely to the background and not to the ion. However, this relies on the readout laser power to remain stable over the scale of detection times, which is on the order of 1 ms, as fluctuations in laser power between shots change the background counts. Therefore, to ensure reliable and controlled readout and cooling of ions, it is required that the laser intensity be stable in time and remain close to a set value. This is done by directing the laser beam through an acousto-optic modulator (AOM), operated in conjunction with a proportional-integral (PI) controller. The laser power is measured with a photodiode, followed by a transimpedance amplifier that converts the photocurrent into a voltage signal. This voltage serves as input to the controller, which generates an output that modulates the radio-frequency (RF) drive applied to the AOM, thereby keeping the laser intensity close to a user-defined reference value. For this case, a power fluctuation of < 2% is desirable for the stable laser.

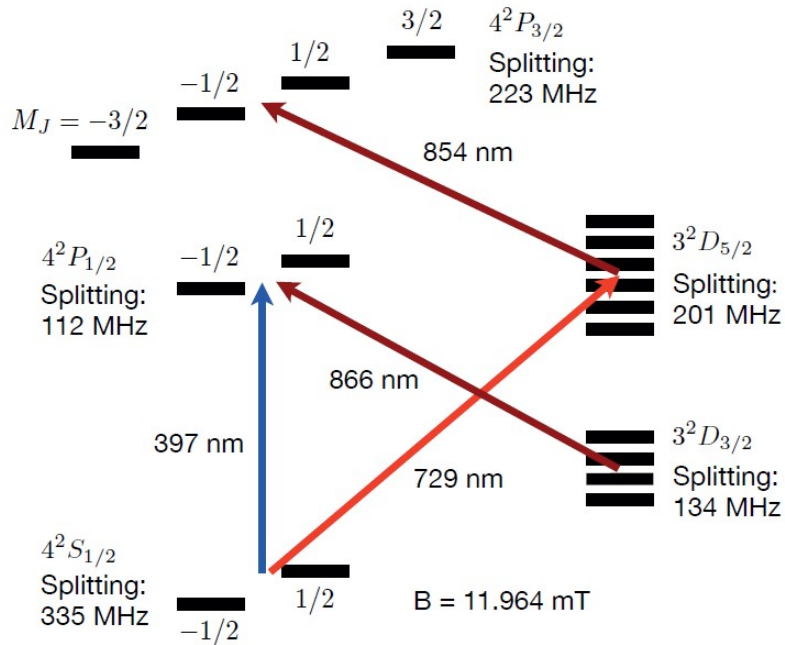


FIGURE 1.1: Energy level diagram for the calcium-40 ion in a magnetic field of 11.964 mT. In the figure, the 397 nm wavelength is used for state readout: the ion fluoresces only if it is in the $4^2S_{1/2}$ state, which is designated as the $|0\rangle$ computational state. The 854 nm laser nm is used for repumping from the $3^2D_{5/2}$ state – assigned as the $|1\rangle$ computational state – to the short lived $4^2P_{3/2}$ state, which subsequently decays to $4^2S_{1/2}$. Additionally, 866 nm light repumps population to the $4^2P_{1/2}$ state. Both repumping beams enable state preparation in the $|0\rangle$ state. The 729 nm laser drives the quadrupole transition from the $|0\rangle$ to $|1\rangle$ state. Figure taken from [7].

Additionally, scaling trapped ion setups to more number of ions necessitates independent control of ions via lasers, which requires multiple independently monitored laser beams. Using a separate laser system for each ion is impractical in terms of hardware and implementation. Therefore, this requires the need to split laser light into multiple beams. For higher wavelengths - such as 729 nm (used for coherent control of Calcium $^{40}Ca^+$ ions), 854 nm (for repumping to the $P_{3/2}$ level), and 866 nm (repumping to the $P_{1/2}$ level), as shown in the level diagram of the calcium-40 ion in Fig.(1.1) – efficient hardware solutions are commercially available such as fiber splitters ([8, 9]). However, for near UV wavelengths, such as 397 nm, this splitting must be achieved using conventional optical components assembled on an optical breadboard.

In this semester thesis, a system for the delivery for the 397 nm laser, including its power stabilization using a single pass AOM configuration, and a 1-to-6 splitting board was completed to enable future experiments on the cryogenic trapped ion setup. The setup comprises a surface ion trap chip that uses integrated photonics with 16 trapping zones. A schematic of the overall beam delivery setup assembled in the project is depicted in Fig.(1.2).

Organization of the Thesis

This thesis is organized as follows. Chapter 2 provides a brief overview of the theory behind acousto-optic modulators, as well as the single-pass and double-pass configurations of the AOM board. Chapter 3 contains theory and discussion on the stabilization of laser power implemented with an AOM and a PI controller. The characterization of the controller is then discussed in the context of noise bandwidth rejection. Finally, chapter 4 describes the design and assembly of the splitting board. This is followed by some remarks on potential exploration and improvements in the current setup, concluding with a summary.

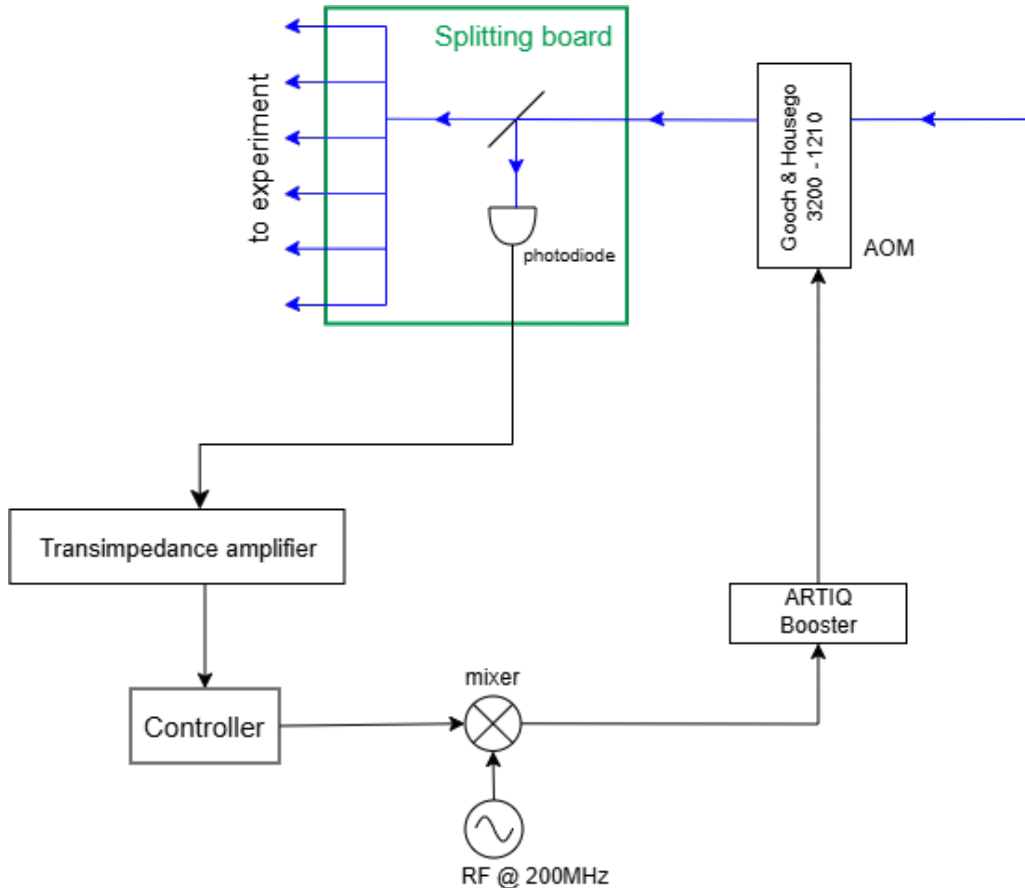


FIGURE 1.2: A schematic of the beam delivery setup. The AOM is used for intensity stabilization by modulating its RF drive. The photodiode, in combination with a transimpedance amplifier, acts as a sensor for laser light, converting the laser signal into a voltage that acts as the input to the controller. The controller's output is multiplied with a 200 MHz RF sinusoidal signal using an RF mixer. Since, the mixer output is not strong enough to directly drive the AOM, it is amplified by the ARTIQ SINARA Booster before being fed to the AOM. This completes the feedback loop. The splitting board splits the laser beam into six different beams, which are directed to the trapped ion experimental setup.

Chapter 2

The Acousto-Optic Modulator

2.1 Theory

An acousto-optic modulator (AOM) is a device that shifts the frequency of incident light using radio frequency sound waves. AOMs are extensively used in experiments that require controlling the intensity of incoming laser light and changing its frequency. In trapped ion experiments, they are often used in the so-called double-pass configuration, which facilitates high-frequency tunability and high extinction ratios [10]. An AOM comprises a transparent crystal through which the light propagates. A piezoelectric transducer attached to the crystal is excited by a sinusoidally oscillating electrical signal from an RF driver. The piezo transducer then excites a sound wave with a frequency of the order of 100 MHz and with an acoustic power of the order of 1 W to 10 W. This sound wave generates a traveling strain wave in the material. The photo-elastic effect, that is, the change in refractive index caused by stress [11], leads to a traveling refractive index grating, which then causes light to experience Bragg diffraction [12]. Most AOMs have an in-built impedance matching circuit to maximize the transfer of RF power from the driver to the crystal.

Let ω_i and ω_a be the angular frequencies of the incident light beam and the acoustic wave respectively. If the interaction length L between the acoustic wave and the light wave is large enough then Bragg refraction occurs and the interaction can be treated as diffraction off a Bragg grating. Specifically, the Bragg regime dominates when $Q = \frac{2\pi}{n} \frac{\lambda_i L}{\lambda_a^2} > 7$, where λ_i is the optical (incident) wavelength, n the index of refraction of the medium, and λ_a the wavelength of the acoustic wave [13]. This is depicted in Fig.(2.1),

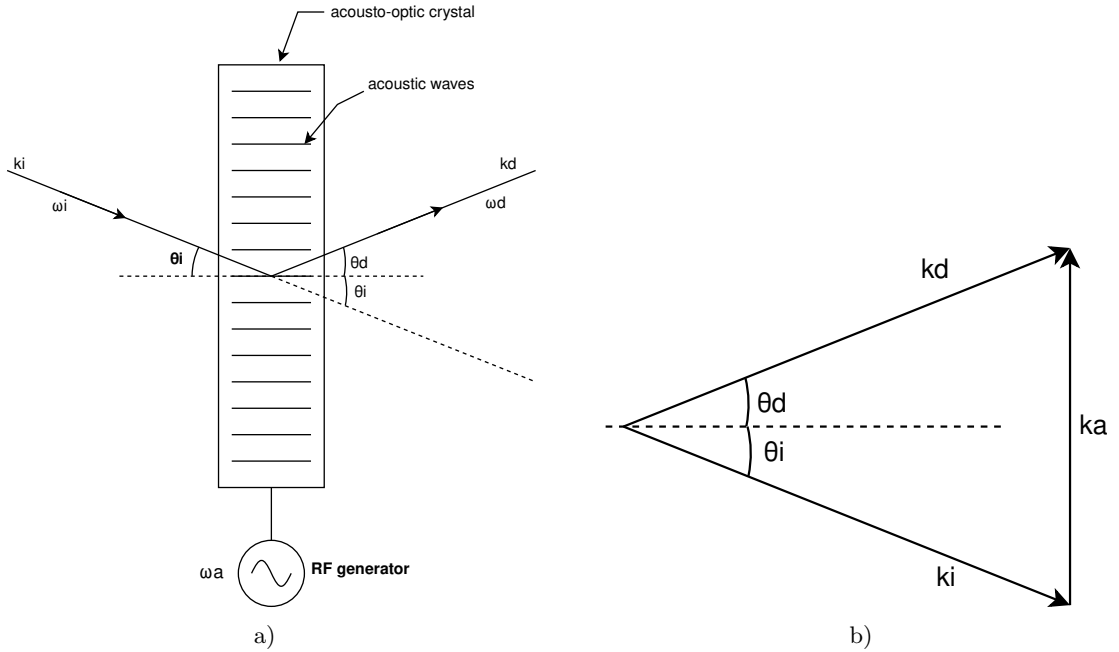


FIGURE 2.1: a) Schematic of an acousto-optic device. The acoustic waves produced by the RF source change the frequency of the incoming light and also deflects it obeying conservation of momentum. b) Wavevectors of the incident (\vec{k}_i) and deflected (\vec{k}_d) optical beams, and of the acoustic wave phonon (\vec{k}_a).

Furthermore, conservation of momentum dictates that the momentum of the deflected beam (\vec{k}_d) is the vector sum of the incident beam (\vec{k}_i) and the phonon (\vec{k}_a), as illustrated in Fig.(2.1(b)). The energy of the acoustic wave is much smaller than that of the light wave, and therefore it is reasonable to assume that $|\vec{k}_i| = |\vec{k}_d|$. This implies $\theta_i = \theta_d = \theta$. This gives the Bragg condition $\sin(\theta) = \frac{\lambda_i}{2\lambda_a}$. This results in angle-separated diffracted beams at frequencies $\omega_i \pm n\omega_a$, where n is an integer, emerging from the AOM, as shown in Fig.(2.3), alongside the (undiffracted) transmitted beam. The transmitted beam that does not undergo any deflection is referred to as the 0^{th} order beam and does not experience a frequency shift whereas other diffraction orders are referred to as the $\pm n^{th}$ orders. The direction of deflection of the positive orders is in the direction of propagation of the acoustic wave and the opposite direction for negative orders. For more detail, [13] provides a good explanation in this regard.

The single-pass and double-pass configurations will now be discussed along with the details of the experimental setup.

2.2 The Single-pass Configuration

The single-pass configuration refers to an arrangement in which light is passed only once through the AOM crystal. For purposes of familiarization, the single-pass configuration was first tested with a 635 nm diode laser on a pre-machined double-pass AOM board as shown in Fig.(2.2). The board in Fig.(2.2) was originally designed for the 729 nm laser. However, it works adequately at 635 nm as well for demonstration purposes.

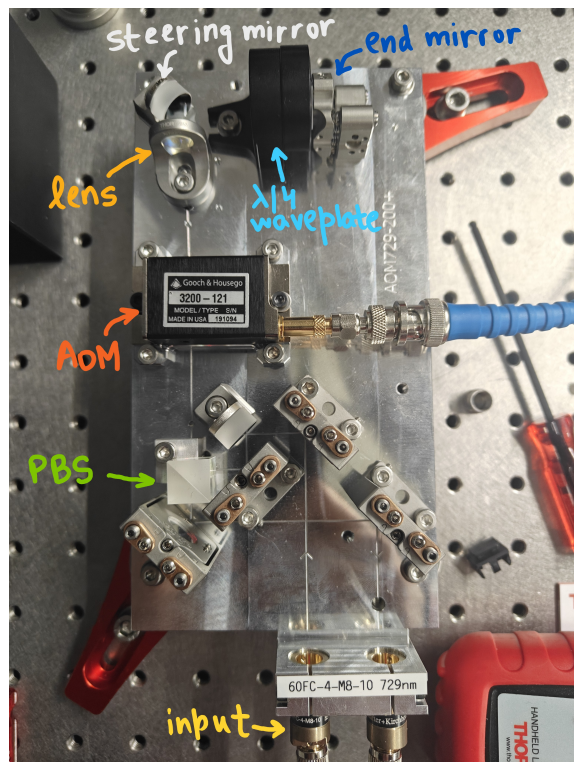


FIGURE 2.2: The double pass AOM board used for in single-pass configuration. This board was originally designed for the 729 nm wavelength as visible on the label in the lower half of the image.

To use the double-pass AOM board in a single-pass configuration, the focusing lens and mirror (visible in Fig.(2.2) near the upper left corner) were removed. Fig.(2.3) shows the diffraction pattern observed when an RF drive signal of 29 dBm is applied to the AOM. The signal is generated using the Moku:Pro and subsequently passed through an RF amplifier.

For the purpose of the project, the single-pass configuration is used for the intensity stabilization of the incoming laser. The details of the feedback loop have been discussed in detail in Section 3.2.

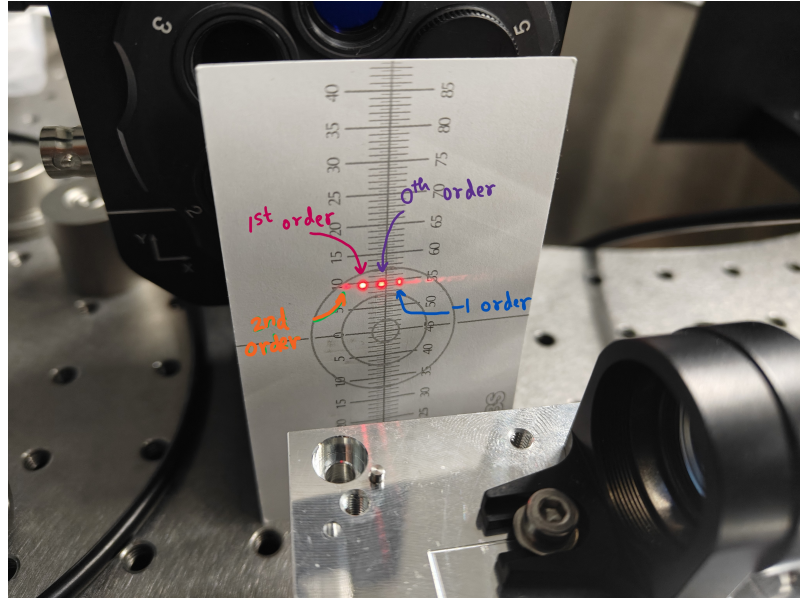


FIGURE 2.3: Diffraction fringes obtained from the single-pass configuration using the 635 nm diode laser. Different diffraction orders are labeled in the figure. The 0th order fringe corresponds to the undiffracted beam, identifiable when the RF drive to the AOM is turned OFF. Positive orders appear in the direction of the propagating acoustic waves i.e., away from the RF drive input.

2.3 The Double-pass Configuration

In the double-pass configuration, light passes through the same AOM twice. This is done through the so-called cat's eye retroreflector configuration comprising a lens placed one focal length away from the output port of the AOM (after the first pass) and a mirror that reflects the light back into the AOM for the second pass. The lens serves to collimate the light emerging from the AOM after the first pass, which consists of beams with different deflection angles. The lens focuses the light so that maximum diffraction efficiency is achieved in the second pass. The configuration also includes a mirror oriented at a 45° angle to guide light toward the end mirror, as well as a quarter waveplate, the function of which is described in the following text. All of these components are visible in Fig.(2.2).

The light coming out from the second pass overlaps with the incoming beam. Different schemes are employed to distinguish between the overlapping input and output light, depending on the wavelength in use. Polarization separation is used for 729 nm, where a quarter waveplate (visible as a black mount in the upper half of Fig.(2.2)) is placed after the AOM, and a polarizing beam splitter (also visible in Fig.(2.2)) is placed before the AOM. This ensures that the second-pass beam has a polarization orthogonal to the input beam and can be 'filtered' by the polarizing beam splitter. On the other hand, height

separation is used for 397 nm: the last mirror (visible in Fig.(2.2) after the quarter-wave plate) is replaced with a prism which changes the height of the reflected beam.

The double-pass configuration carries the benefit of additional frequency tunability since the fringe corresponding to a shift equal to $2\omega_a$ is kept while others are discarded. In order to see the fringes resulting from the double pass of light, the mirror at the lower left corner in Fig.(2.2) is removed and the fringes can be seen on the surface of a beam block in Fig.(2.4):



FIGURE 2.4: A picture of the diffraction pattern. The brightest spot is the $+1^{st}$ order diffraction spot. To its left is the $+2^{nd}$ order spot while to its right are the 0^{th} and -1^{st} order fringes.

Although, the assembly and configuration of the double-pass AOM boards was not done as part of this semester project, it is still worth mentioning since each of the six beams at the output of the splitting board passes through six such boards before being sent to the ion trap setup. The AOM boards thus enable fast switching of the laser light and allow independent control of individual beams incident on the ions. In addition, the RF drive frequency of each board can be independently adjusted to shift the laser frequency for readout and cooling.

Chapter 3

Laser Intensity Stabilization

As mentioned in Chapter 1, stable laser power is necessary for precise readout and Doppler cooling of calcium ions. Stable laser power is achieved through continuous regulation of the RF drive that excites the AOM crystal via a feedback loop, thereby maintaining a constant intensity in the 0th order fringe at the output of the AOM. As discussed in Chapter 2, the 0th order fringe remains unchanged in frequency and is thus sent to the trapped ion setup, while the remaining diffraction orders are dumped.

In this chapter, the basics of control theory are reviewed. This is followed by a discussion on one of the widely used schemes in control theory, namely the proportional-integral-derivative (PID) controller. The experimental configuration is then presented along with details on setting up such a controller for laser intensity stabilization.

3.1 Fundamentals of Control Theory

Working with control systems often involves handling differential equations with integral and derivative terms. The Laplace transform is a mathematical tool that simplifies differential equations by writing them as algebraic equations. The Laplace transform of a function $f(t)$ is given by $\mathcal{L}[f(t)]$:

$$\mathcal{L}[f(t)](s) = F(s) = \int_0^{\infty} f(t)e^{-st}dt, \quad (3.1)$$

where $s = \sigma + j\omega$ is a complex variable.

Any control system has the following elements:

- Plant (or process): the plant is a system whose output is to be controlled e.g., a DC motor that dictates the motion of a robotic arm. In this case, it is the AOM.
- Controller: a device that generates a controlled input that affects the system output e.g., the PI controller in this experiment that generates a voltage which changes the input to the AOM.
- Sensor: measures the output of the plant and feeds it to the controller in a form used by the controller e.g., the water level inside a washing machine may be measured and converted into an electrical signal for the controller which determines if more water is needed. In this experiment, the photodiode acts as the sensor. Note that the photodiode generates a current, and therefore a transimpedance amplifier is required to convert this current into a corresponding voltage that can be used by the feedback loop.

The block diagram of a generic closed-loop control system is given in Fig.(3.1).

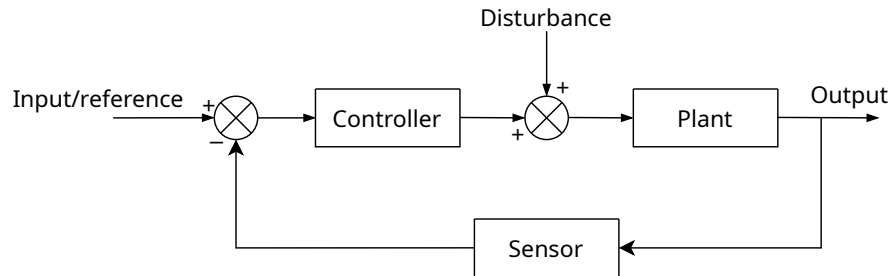


FIGURE 3.1: A closed-loop control system. In the context of the experimental setup, the plant is the AOM, and the sensor comprises the photodiode and transimpedance amplifier. The reference signal is a user-defined DC voltage, chosen to be lower than the minimum voltage value of the ‘raw’ unstable laser. Disturbances may arise from drifts in polarization, temperature fluctuations in the laboratory, vibrations or mechanical disturbances such as other people working in the vicinity of the setup.

For linear, time-invariant systems, it is common practice to use the *transfer function*, which is defined as the ratio of the Laplace transform of the output and the Laplace transform of the input. Consider, for a general linear, time-invariant system, the relation between the input $x(t)$ and the output $y(t)$ given by,

$$a_n \frac{d^n y(t)}{dt^n} + a_{n-1} \frac{d^{n-1} y(t)}{dt^{n-1}} + \dots + a_0 y(t) = b_m \frac{d^m x(t)}{dt^m} + b_{m-1} \frac{d^{m-1} x(t)}{dt^{m-1}} + \dots + b_0 x(t) \quad (3.2)$$

Taking the Laplace transform on both sides,

$$\begin{aligned} & a_n s^n Y(s) + a_{n-1} s^{n-1} Y(s) + \dots + a_0 Y(s) + (\text{derivative terms of } y(t) \text{ at } t=0) \\ & = b_m s^m X(s) + b_{m-1} s^{m-1} X(s) + \dots + b_0 X(s) + (\text{derivative terms of } x(t) \text{ at } t=0) \end{aligned}$$

Assuming all initial conditions are zero,

$$a_n s^n Y(s) + a_{n-1} s^{n-1} Y(s) + \dots + a_0 Y(s) = b_m s^m X(s) + b_{m-1} s^{m-1} X(s) + \dots + b_0 X(s),$$

then the transfer function $G(s)$ is given by:

$$G(s) := \frac{Y(s)}{X(s)} = \frac{b_m s^m + b_{m-1} s^{m-1} + \dots + b_0}{a_n s^n + a_{n-1} s^{n-1} + \dots + a_0},$$

Let $R(s)$ be the input, $C(s)$ the output, $E(s)$ the Laplace transform of the error signal $e(t)$, and $G(s)$ and $H(s)$ the transfer functions of the plant + controller and sensor respectively in Fig.(3.2). Therefore, the *closed-loop transfer function* for a system shown in Fig.(3.2) is given as,

$$\begin{aligned} E(s) &= R(s) - H(s)C(s) \\ C(s) &= E(s)G(s) \\ \Rightarrow C(s) &= G(s)[R(s) - H(s)C(s)] \\ \Rightarrow \frac{C(s)}{R(s)} &= \frac{G(s)}{1 + H(s)G(s)} \end{aligned} \tag{3.3}$$

where the product $G(s)H(s)$ is the *open-loop transfer function*. The goal of any closed-loop control system, such as the one above, is to keep the output $C(s)$ as close to the input (reference) $R(s)$ as possible.

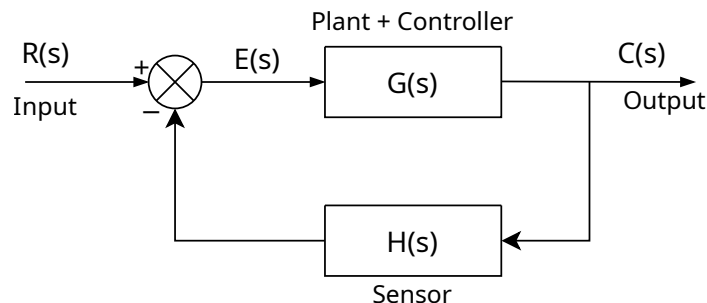


FIGURE 3.2: Schematic of a feedback loop with the plant and controller merged together. Signals are shown as Laplace transforms of their respective time-domain quantities.

However, the use of the transfer function is limited only to systems that can be described by linear differential equations. Therefore, the *state-space representation* finds more use when it comes to studying non-linear systems. The state-space representation shall not be discussed here, since it clouds the key ideas in understanding control theory. [14, 15] are good references in this regard for interested readers.

Note that the output $C(s)$ in Eq.(3.3) is unstable i.e., is unbounded if $1 + H(s)G(s) = 0$. This motivates the introduction of two quantities:

- Gain margin: let there be a point s_g for which $\arg(H(s_g)G(s_g)) = \pi$. Then, the gain margin is defined as the minimum factor by which $G(s)H(s)$ must be changed to make the closed-loop system unstable, i.e. $g = \frac{1}{|G(s_g)H(s_g)|}$. Alternatively, the factor by which $G(s)H(s)$ needs to be multiplied to make the system unstable.
- Phase margin: let s_p be the point where $|G(s_p)H(s_p)| = 1$ then the phase margin is the minimum angle by which the phase of $G(s)H(s)$ needs to be changed for it to have a phase of 180° or -180° .

The following Fig.(3.3) from the textbook Modern Control Engineering by Ogata [16] provides a good pictorial representation of these definitions. The textbook assumes $H(s) = 1$ for its discussion but the key idea remains the same.

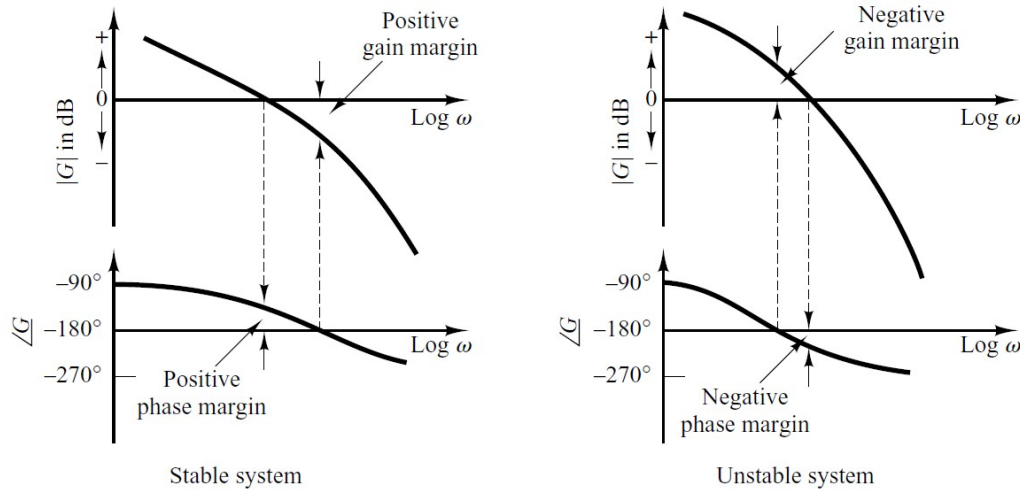


FIGURE 3.3: A heuristic representation of gain and phase margin taken from [16]

3.1.1 The Proportional-Integral-Derivative (PID) Controller

A good controller design takes into account the mathematical model of the plant. However, in most cases, it is difficult to determine an accurate model for the plant and analytical methods cannot be used. This issue is solved using proportional-integral-derivative (PID) controllers. The popularity of PID controllers stems from their tunability and ease of implementation.

The goal is to minimize the error $e(t) = r(t) - y(t)$ where $r(t)$ is the input reference signal and $y(t)$ is the output. The action of a PID can be written as follows [17],

$$\begin{aligned} x(t) &= x_P(t) + x_I(t) + x_D(t) \\ &= K_P e(t) + K_I \int_0^t e(\tau) d\tau + K_D \frac{de(t)}{dt}, \end{aligned}$$

which in transfer function form can be written as,

$$G(s) = K_P + \frac{K_I}{s} + K_D s.$$

Consider the effect of different terms in the above expression,

- **The Proportional Term (K_P):** This term applies a correction that is proportional to the magnitude of the error. A high value of the proportional gain K_P leads to a shorter rise time and a lower steady state error but can also cause the output to oscillate for a longer time. Since the proportional term always requires a non-zero error to be effective, it cannot cancel out the error by itself.
- **The Integral Term (K_I):** This term keeps a memory of the error over previous times. Therefore, a persistent error causes the integral term to increase over time and apply a larger correction. For this reason, the integral term, unlike the proportional term, can apply a correction even when the error is zero and can bring the system to the required set point by itself. An integral term with a higher gain (K_I) will eliminate the error faster than a lower gain. However, care must be taken not to use too high a value for the integrator gain since error accumulation can cause the integrator to become aggressive and lead to oscillations around the set point. This is called integrator windup [18].
- **The Derivative Term (K_D):** The derivative term applies a correction based on the future tendency i.e., slope of the error. This improves the stability and makes

the loop more responsive to changes. However, this term is very sensitive to the input and is omitted in many cases if the input is too noisy or if the sensor used for feedback is not perfect.

The differential gain term is not employed in this implementation due to unreliable sampling of high-frequency noise, and therefore a proportional-integral (PI) controller suffices for this application.

3.2 Experimental Configuration

As mentioned in chapter 2, the RF drive to the AOM results in fringes of different frequencies namely the -1, 0th, 1st, 2nd order and other higher orders. The 0th order fringe corresponds to the beam that is unchanged in frequency and therefore, laser intensity stabilization involves regulating the power in the 0th order fringe. A stronger RF drive (higher amplitude) results in more optical power diffracted into higher-order fringes, reducing the power in the 0th order fringe. Conversely, a lower RF amplitude implies more power in the 0th order fringe. The function of the controller, therefore, is to modulate the RF drive in such a way that the power in the 0th order fringe remains constant (close to a set point) by suitably changing the strength of the RF signal.

For this, the AOM is deployed in the single-pass configuration. It should be made sure that the AOM orientation is done so as to keep the power in 0th fringe to a minimum when the RF drive is ON, which can be done by simply observing the diffraction fringes on a surface. This ensures that the controller has a larger operating window while stabilizing and prevents railing of the controller output.

3.2.1 The Moku:Pro as a PID

For controller tuning and proof-of-concept purposes, the stabilization of the 397 nm laser was first performed on a separate optical table. The schematic of the configuration, along with the actual picture of the setup, is shown in Fig.(3.4),

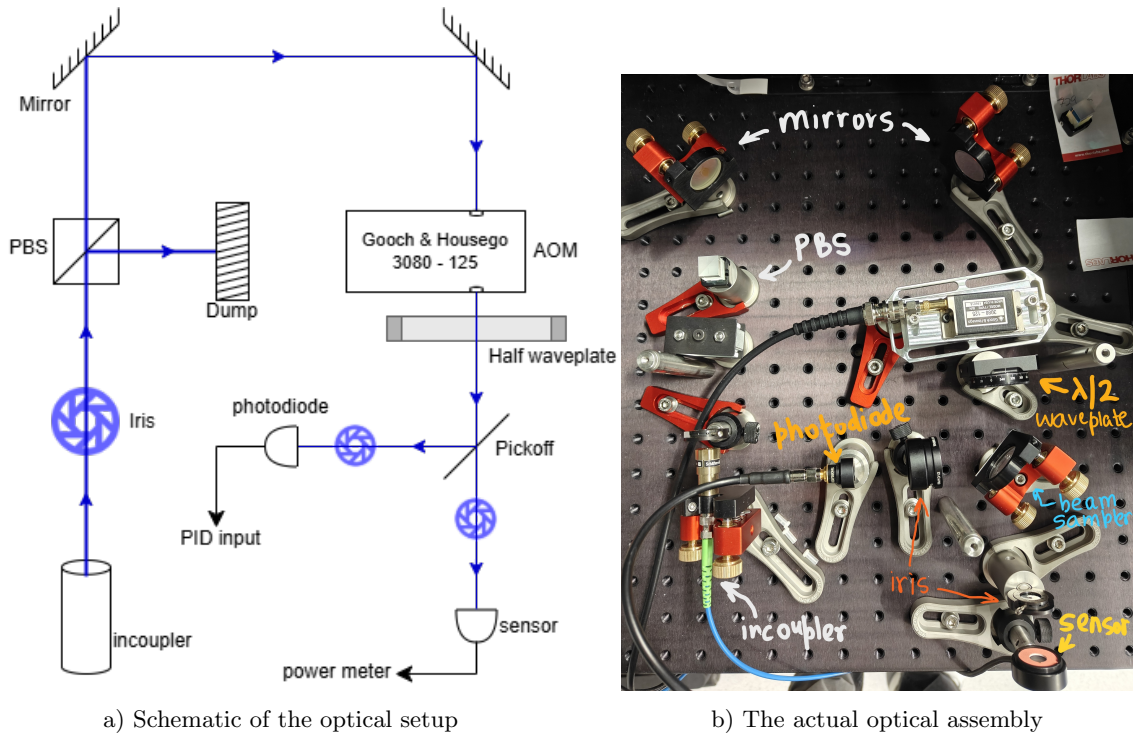


FIGURE 3.4: The optical setup for using the Moku:Pro as a controller. The PBS and half waveplate are used to control the laser power incident on the photodiode and the sensor. Two irises are positioned just before the photodiode and sensor allowing only the 0th order light to pass and blocking higher diffraction orders.

Here, the Moku:Pro's inbuilt PID functionality was used to implement the controller. A small amount of laser power, typically 5-10%, was sampled through a photodiode (Thorlabs SMR05/M) using a pickoff and sent through a transimpedance amplifier (Thorlabs AMP120) to one of the inputs of the Moku. The output of the Moku is an amplitude modulated RF wave at a frequency of 80MHz and an original amplitude of $0.398V_{pp}$. The output of the Moku is not strong enough to drive the AOM and has to be first passed through an RF amplifier (Mini-Circuits ZHL-1-2W-S+) which provides a gain of $+29dBm$ and then to the AOM (Gooch & Housego 3080-125). A heuristic approach was employed to tune the PI controller. This was done by starting with a low integrator crossover frequency, typically around 10 Hz, which was gradually increased while continuously monitoring the laser signal on an oscilloscope to see if the signal was being stabilized. A proportional gain was introduced as needed, based on its effect in improving signal fluctuation. Using this method a proportional gain of $23 dB$ and an integrator crossover frequency of $60 Hz$ was found to be optimal. It should be noted that formal tuning methods, such as the Ziegler-Nichols method or similar approaches, can also be applied, but are not strictly required.

The laser signal is recorded through the other (transmitted) output of the pickoff using a Thorlabs S121C power sensor and a power meter. The data logging is done using the Moku:Pro. Although the Moku features a GUI software, its PID functionality, data logging, and the RF generator were controlled using a python script to facilitate automation.

The signal level from the photosensor is recorded both for short (5 minutes) and long durations (3 hours) to test the reliability of the feedback loop. In the latter case, data is collected for a window of 60 seconds every 10 minutes. This sequence is repeated for three hours. The data for the former and latter cases are given in Fig.(3.5) and Fig.(3.6) respectively,

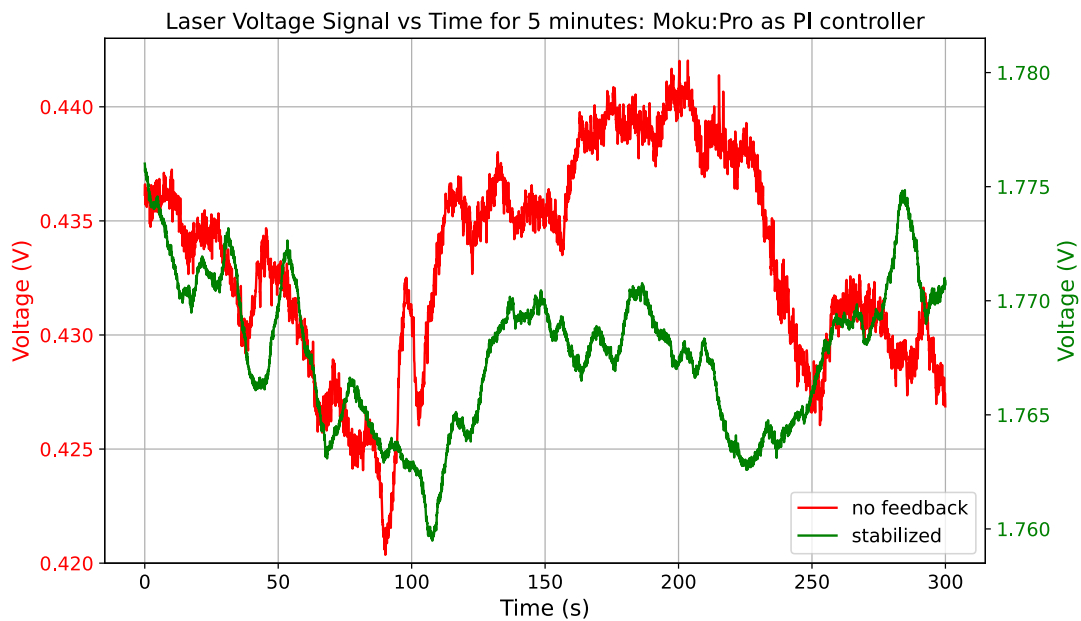


FIGURE 3.5: Photosensor voltage signal (for the laser) collected over five minutes. The red curve is the unstable ‘raw’ laser signal and the green curve is the laser signal with the controller ON. These data were collected sequentially and not simultaneously. Note the reduction in high frequency fluctuations in the stabilized signal (green) compared to the original laser signal (red).

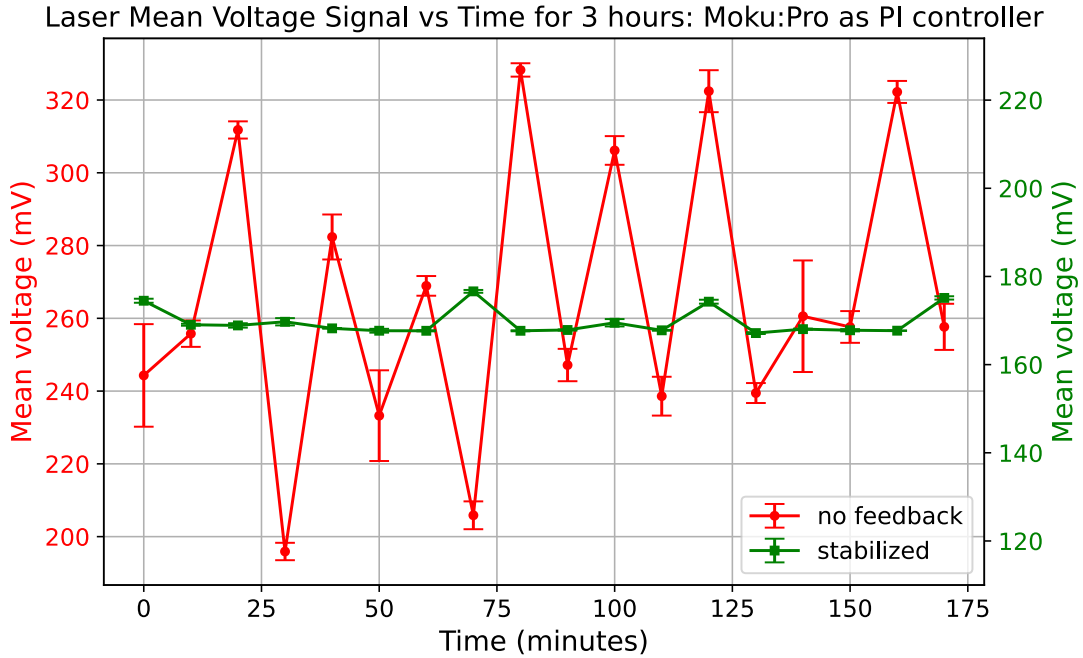


FIGURE 3.6: The mean voltage level from the photosensor-powermeter collected over three hours. The red curve shows the ‘raw’ laser signal level, and the green curve shows the signal with the feedback loop enabled. Each data point is the mean of the voltage readings from the photosensor-powermeter collected over 60 seconds. Error bars are indicative of the laser signal variation within the sixty-second window.

The percentage fluctuation of the laser signal can be calculated as $\frac{P_{max} - P_{min}}{P_{mean}} \times 100$, where the respective quantities denote the maximum, minimum and mean powers in the recorded data. From Fig.(3.5), the unstable ‘raw’ laser power has fluctuations up to $\approx 5\%$. Whereas, the stabilized laser power fluctuates on the order of $\approx 0.93\%$. Similarly, from Fig.(3.6), the ‘raw’ laser power has fluctuations up to $\approx 50\%$, and the stabilized laser power fluctuates on the order of $\approx 5\%$. These relatively large fluctuations in the latter case may be due to the laser not being locked at the time of data collection.

3.2.2 The SINARA Stabilizer as a PID

As a long-term implementation, it is preferable to use the ARTIQ SINARA Stabilizer board as the feedback controller. The stabilizer board features inbuilt biquadratic infinite impulse response (IIR) filters. IIR filters are known to be flexible and have the ability to be configured as PID controllers. This requires converting the parameters calculated in the previous section to IIR parameters that are accepted by the SINARA. The stabilizer parameters can be passed either through the MQTT Explorer interface or through a python

script. The following Github repository [19] serves as a guide to set up the SINARA Stabilizer. The following webpage [20] is an excellent reference for using an IIR filter as a PID controller.

A brief explanation on controller-to-IIR parameter conversion is given below:

PID to IIR Parameters Conversion

Consider the IIR filter given in Fig.(3.7) as a black box with input x and output y . Let the three most recent inputs x_0, x_1, x_2 and the two most recent outputs y_1, y_2 of the IIR be available. Then the combination of the feedforward and the feedback expressions give,

$$y_0 = y_1 + (k_P + k_I + k_D)x_0 - (k_P + 2k_D)x_1 + k_Dx_2 + u \quad (3.4)$$

$$= b_0x_0 + b_1x_1 + b_2x_2 - a_1y_1 - a_2y_2 + u, \quad (3.5)$$

here u is the offset term which is decided by the reference point of the controller. The core of the IIR uses 16-bit signed integers, and therefore the scaling is given by $1 << 15 - 1 = 2^{15} - 1 = 32767$, where $M << N$ indicates shifting of the binary number M by N places to the left. The offset u is then calculated from the setpoint voltage $V_{setpoint} > 0$ (in volts) as: $u = -\frac{32767}{10} \times (b_2 + b_1 + b_0) \times V_{setpoint}$. This relation can be explained with context to Fig.(3.7). An offset voltage is multiplied by $(b_0 + b_1 + b_2)$ before appearing in the output. This offset value is negative, as the error must be brought close to zero. The minimum and maximum voltages that the SINARA can output are given by an integer between -32767 and 32767 which corresponds to a voltage between -10 V and 10 V , respectively. This explains the presence of the scaling factor given by $\frac{32767}{10}$.

Consider the transfer function of a PI controller: $G(s) = K_P + \frac{K_I}{s}$. Using Tustin's transformation: $s \rightarrow \frac{2}{T_s} \frac{1-z^{-1}}{1+z^{-1}}$ [21], the discrete transfer function $G(z)$, after simplification, can be written as:

$$G(z) = \frac{K_P + K_IT_s/2 + z^{-1}(-K_P + K_IT_s/2)}{1 - z^{-1}}$$

Comparing this with the discrete form for the biquadratic filter, $H(z) = \frac{b_0 + b_1 z^{-1} + b_2 z^{-2}}{1 + a_1 z^{-1} + a_2 z^{-2}}$, the following relations can be obtained:

$$\begin{aligned} b_0 &= K_P + \frac{K_I T_s}{2}, \quad b_1 = -K_P + \frac{K_I T_s}{2}, \quad b_2 = 0, \\ a_1 &= -1, \quad a_2 = 0, \end{aligned}$$

here T_s is the sampling time for the SINARA and is roughly $1.3 \mu\text{s}$ as mentioned in [19].

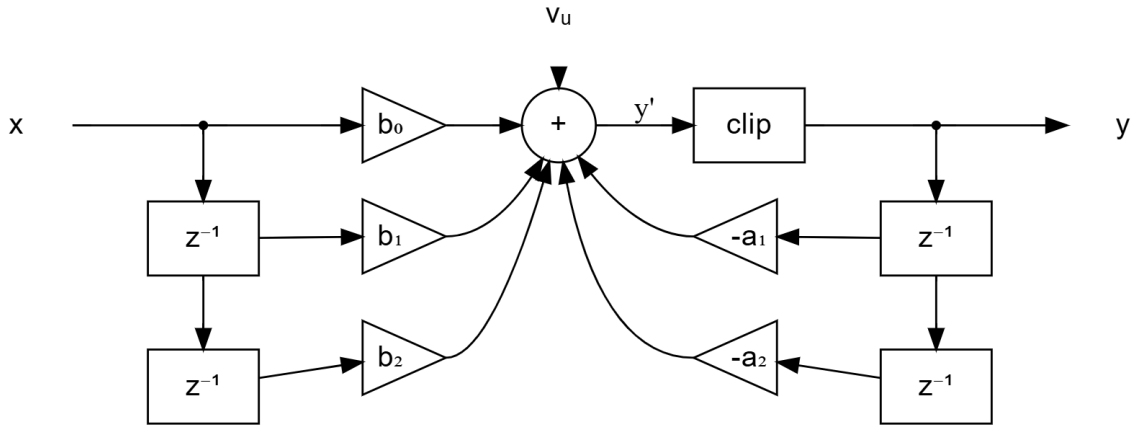


FIGURE 3.7: A schematic representation of a biquadratic IIR filter. Taken from [20].

The same optical setup as that in Section(3.2.1) is used to test the SINARA. However, now instead of directly amplitude modulating the RF output from the Moku, an RF mixer (Mini-Circuits Mixer ZLW-3+) is used to multiply the RF drive (connected to input L of the mixer) with the controller output (connected to input I of the mixer). The output of the mixer then goes through the RF amplifier, which then drives the AOM. The signal level from the photosensor is recorded again for both short (120 seconds) and long durations (3 hours). The data for the former and latter is given in Fig.(3.8) and Fig.(3.9) respectively.

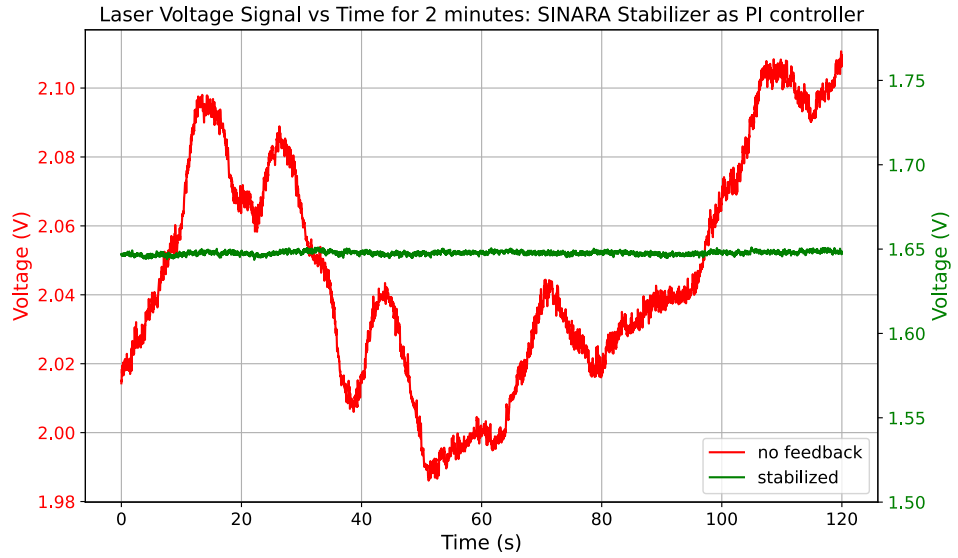


FIGURE 3.8: The voltage level from the photosensor-powermeter is plotted over two minutes. The red curve shows the ‘raw’ laser signal level without the feedback, and the green curve shows the signal with the controller ON.

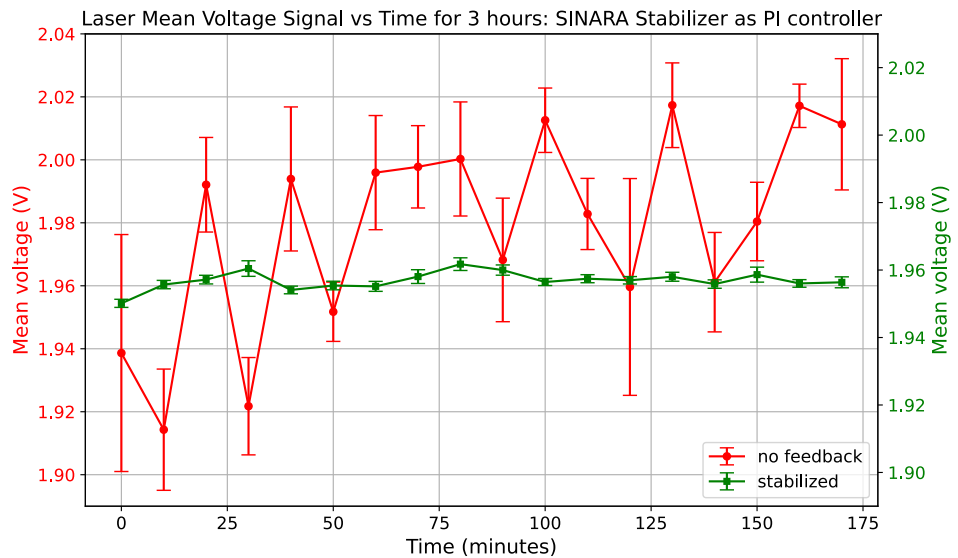


FIGURE 3.9: The mean voltage level from the photosensor-powermeter is plotted over a duration of three hours. The method of collection remains the same as that mentioned in the caption of Fig.(3.6). The red curve shows the laser signal level without the stabilization, and the green curve shows the signal with the controller ON. It should be noted that the error bars are much smaller for when feedback is enabled which indicates lower power fluctuations within the sixty second data collection window as well.

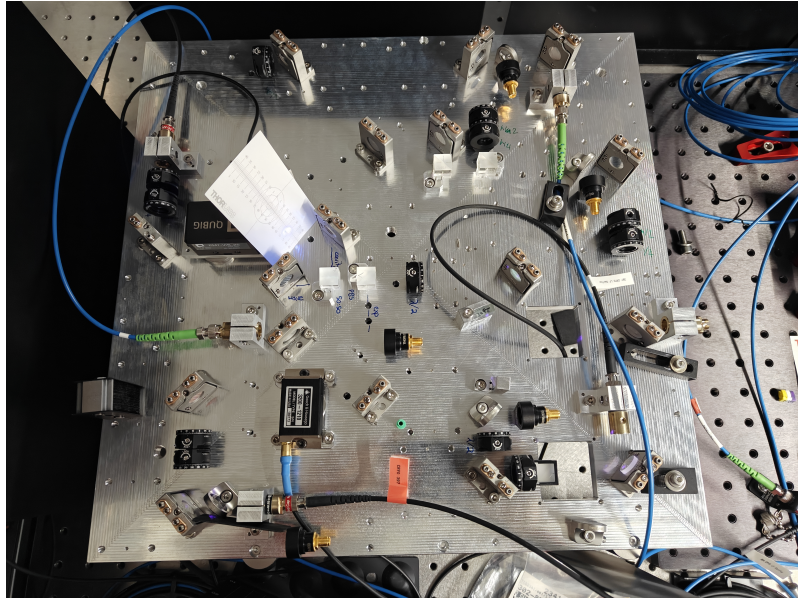


FIGURE 3.10: The splitting board used to send light to the experimental setup and to the cavity for locking the laser. The AOM used for the power stabilization is visible near the lower left of the board.

From Fig.(3.8), the percentage fluctuation of intensity in the unstable beam can be estimated as $\approx 6\%$, while it is $\approx 0.4\%$ for the stabilized beam. From Fig.(3.9), the percentage intensity fluctuation in the unstable beam is $\approx 5.2\%$, while it is $\approx 0.6\%$ for the stabilized beam.

The stabilization setup was moved to the final splitting board directly after the laser source (shown in Fig.(3.10)), which uses a Goooch & Housego 3200 - 1210 AOM with a center frequency of 200 *MHz*. The reference signal is now sampled from the photodiode PD0 on the splitting board, visible in Fig.(4.1) and Fig.(4.2). The RF amplifier is now replaced with the SINARA Booster which offers a constant gain of +29 dBm to the input RF wave. The remaining configuration of the setup is unchanged.

3.3 Noise Rejection Bandwidth

The noise rejection bandwidth gives a measure of the noise rejection performance of a control loop. Sinusoidal noise of amplitude 50 *mV* is intentionally injected into the control loop and added to the controller output signal as shown in Fig.(3.11). The key principle is that the controller compensates for the injected noise, causing the laser signal to oscillate 180° out of phase with the applied sinusoidal disturbance. For this case, the configuration shown in Fig.(3.11) was employed.

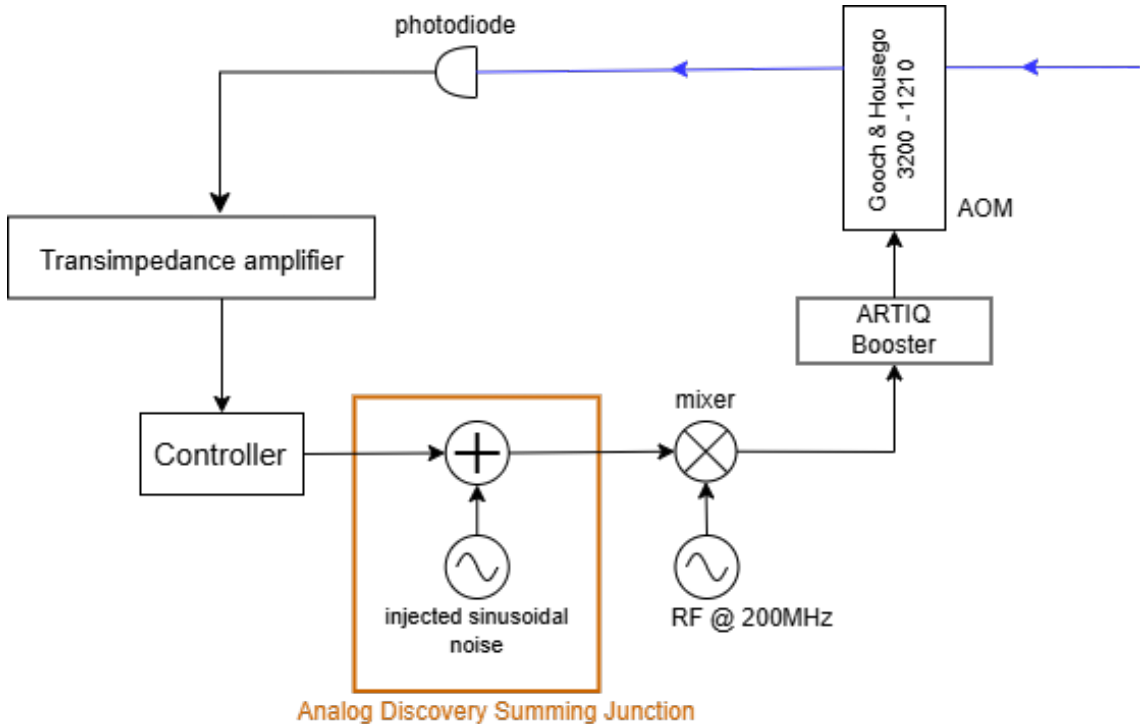


FIGURE 3.11: A schematic of the setup used for probing noise rejection. Sinusoidal noise of up to 100 mV amplitude is added to the output of the controller and then fed to the AOM through the mixer and the booster. The blue line indicates the laser beam.

The signal addition was done using the Analog Discovery Summing Junction controlled through a Digilent Analog Discovery 2 board. The summing junction is a custom PCB designed at ETH which can be used in conjunction with the Digilent Analog Discovery board. The Digilent Analog Discovery has inbuilt $\pm 5\text{ V}$ power supplies and waveform generators that can be used to artificially inject noise into the system. The frequency response i.e., gain vs. frequency and phase vs. frequency of the controller output is recorded through the Network Analyzer functionality of the Digilent Waveforms software.

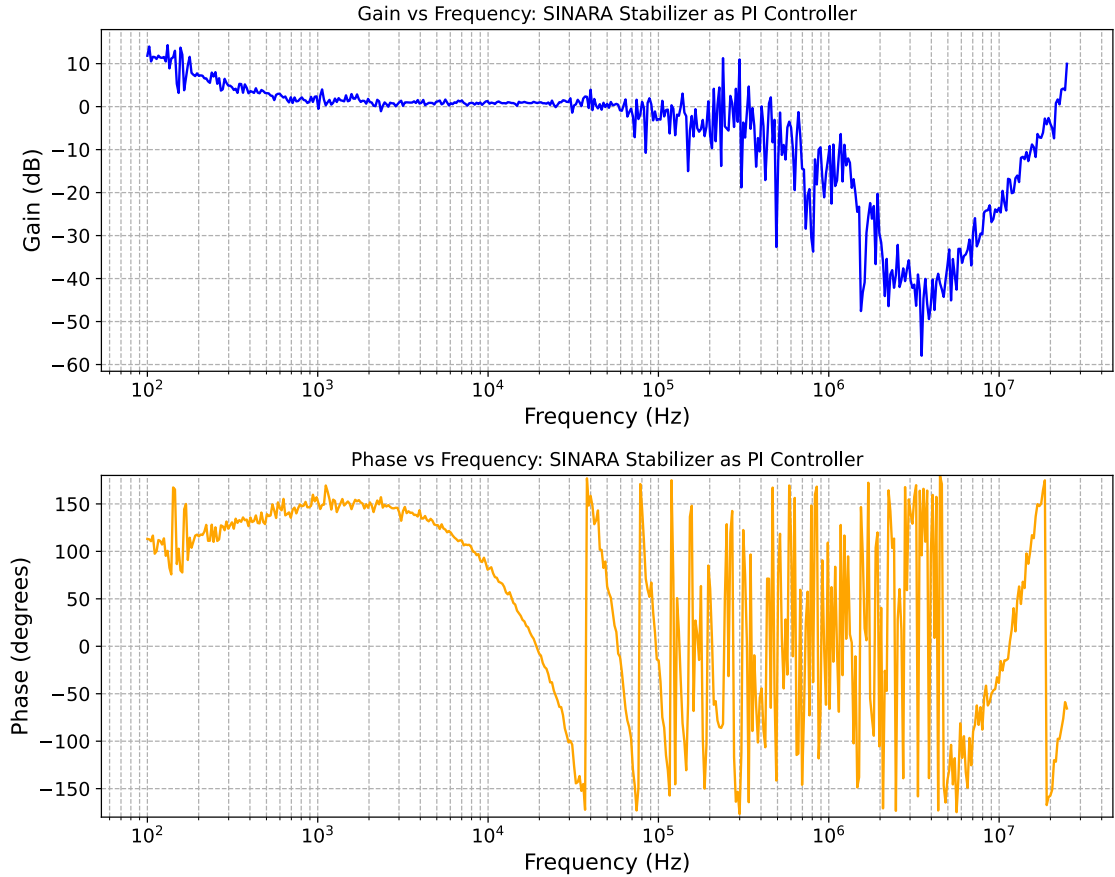


FIGURE 3.12: Gain and phase plots versus frequency at a noise amplitude of 100 mV_{pp} for the SINARA Stabilizer. The loop exhibits unstable behavior for $f > 40 \text{ kHz}$ as evident from the phase versus frequency plot.

It is observed that the control loop demonstrates unstable behavior beyond 40 kHz , as can be seen in the phase versus frequency plot in Fig.(3.12). The reason for this is the high latency of the stabilizer, as was verified separately by measuring the delay between the input and the output of the stabilizer, which was found to be $25 \mu\text{s}$. This explains the behavior of the plots seen in Fig.(3.12).

This large latency can be attributed to a larger batch size in the dual-iir Rust source code file [22]. A larger batch size leads to a longer delay. However, reducing the batch size causes the SINARA output to become unstable. This can be mitigated by lowering the sampling rate of the analog-to-digital converter. Due to time constraints in the project, it was not possible to explore in detail the nuances of using different batch sizes. However, this topic has previously been examined by other members of the laboratory.

Furthermore, to verify the controller design, a similar noise rejection bandwidth measurement was carried out using the Moku:Pro's PI controller. The following measurement results were obtained:

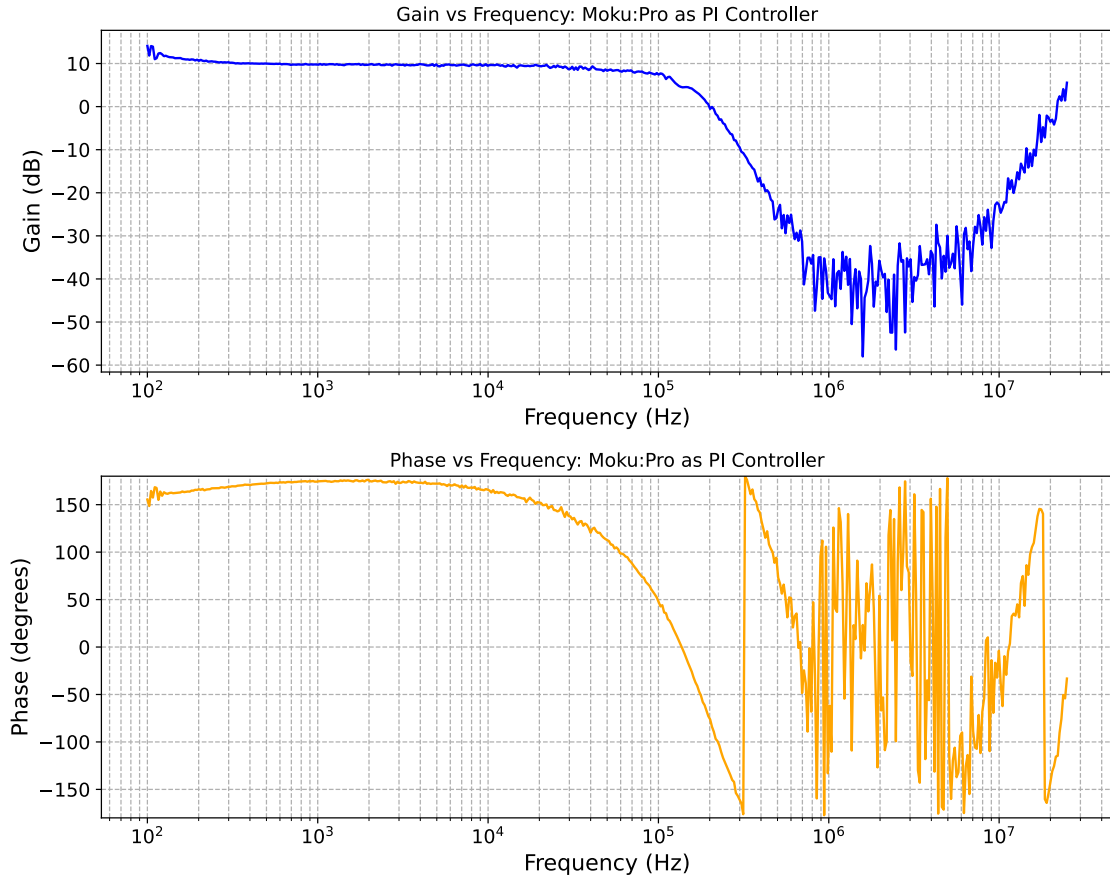


FIGURE 3.13: Gain and phase plots versus frequency at a noise amplitude of 100 mV_{pp} for the Moku:Pro configured as a PI controller.

It is observed from the phase versus frequency plot in Fig.(3.13) that the loop exhibits instability beyond 300 kHz . This confirms that the SINARA's high latency is the limiting factor for the bandwidth.

Chapter 4

The Splitting Board

To facilitate multi-zone addressing of ions, the implementation of a 1-to-6 splitting board for the 397nm was done.

4.1 Design

The design of the board was done considering constraints of the physical size of the mounting rack. A first design was made using OptiSketch, which is a custom module written in python. The design is shown in Fig.(4.1). The dimensions of the optical breadboard were estimated to be $40 \times 30 \text{ cm}$.

Splitting is achieved using lambda half waveplates and polarizing beam splitters (PBS) and light is directed into output couplers using mirrors. The half waveplate is placed before each PBS, which can be rotated to change the polarization direction of the incoming beam. By rotating the half waveplates, the power distribution between the output paths can be finely controlled, allowing for balanced optical power sent to each output.

4.2 Hardware Considerations During Assembly

The choice of the input collimator (incoupler) is dictated by constraints on the beam diameter. The beam diameter is dictated by the fibers being used for outcoupling¹. This fiber has an effective numerical aperture of $NA_{e2} = 0.07$ at 405 nm [23]. The beam

¹OPM-11-405-3/125-P-3A3A-1-0.8-4-SI-TO18 from OZ Optics

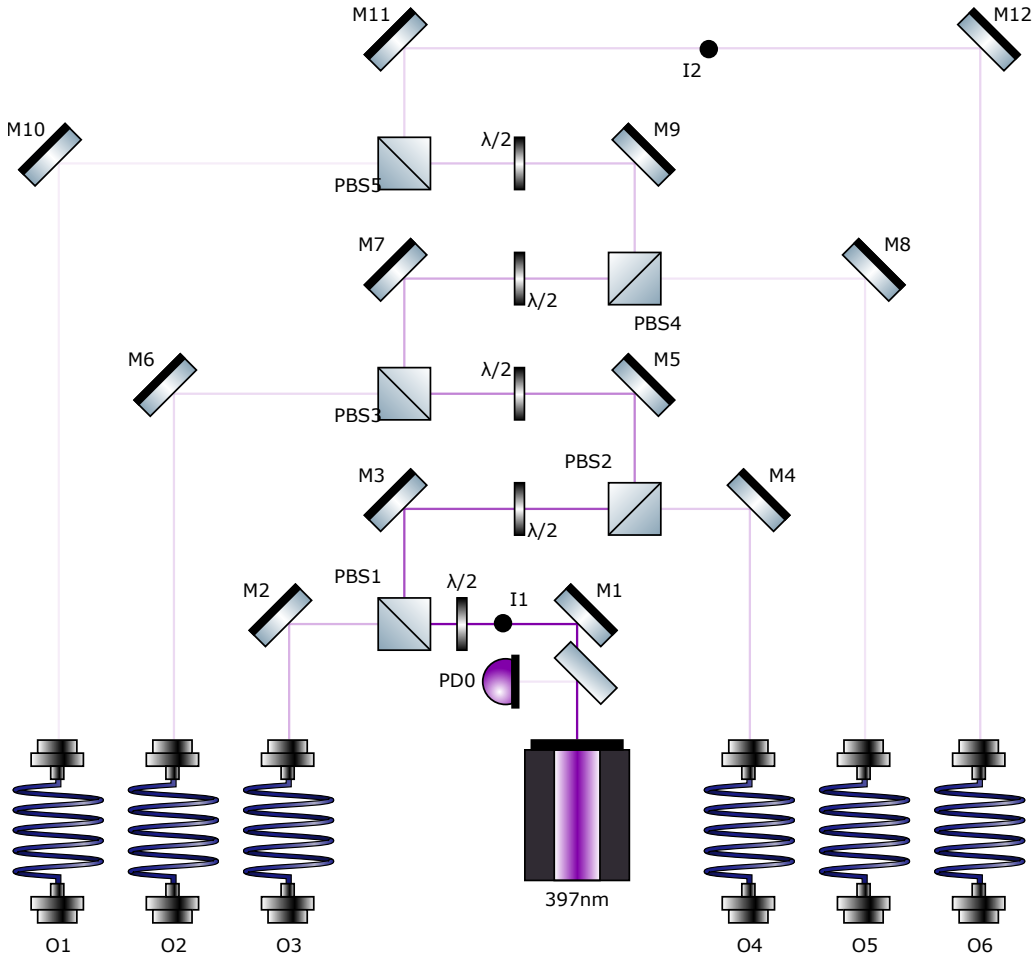


FIGURE 4.1: A schematic of the splitting board. $M_1 - M_{12}$ indicate mirrors, $PBS_1 - PBS_5$ stand for polarizing beam splitters, $O_1 - O_6$ are the output collimators (outcouplers), I_1 and I_2 are irises, $PD0$ indicates the beam sampler and photodiode, and labels $\lambda/2$ indicate half wavelplates.

diameter ϕ_{beam} is then calculated as $\phi_{beam} = 2f'NA_{e^2}$ for the focal length f' dictated by the outcoupler, $f' = 8\text{ mm}$ in this case. This gives a beam diameter of $\phi_{beam} = 1.12\text{ mm}$.

The input coupler is selected by calculating the required focal length of the incoupler: $f' = \frac{0.5\phi_{beam}}{NA_{e^2}}$. Here, the effective numerical aperture is $NA_{e^2} = 0.084$ for the input fiber². This gives a focal length of $f' = \frac{0.5 \times 1.12}{0.084} = 6.66\text{ mm}$, which is close to 7.5 mm . The Schäfter+Kirchhoff 60FC-4-A7.5-01 is thus chosen as the input collimator. The input fiber is an end cap that is crucial in mitigating the effects resulting from high laser powers [24].

²Schäfter+Kirchoff PMC-360Si-3-28E-1000

Note that for Schäfter+Kirchhoff, “A7.5” indicates the type of lens assembly (“A” stands for aspheric) and the focal length (“7.5” indicates a focal length of 7.5 mm). A collimator with an aspheric lens is desirable at the input due to its ability to withstand high laser powers. In contrast, doublet optics collimators (indicated with “M” in the case of Schäfter+Kirchhoff) degrade over time as a result of intense UV exposure to adhesives present within the optical assembly of the collimator. However, a type A collimator at the input was found to cause concentric rings in the beam profile, as also indicated in the documentation [25]. Additionally, the beam suffered from nonuniform beam diameter at each of the outputs even after focusing. However, because the application requires high powers in the UV range, type A collimators are still favorable for long-term use compared to type M collimators. Moreover, differences in beam diameter can be later corrected through lenses.

To summarize, the following couplers and fibers were used in the design:

- Schäfter+Kirchoff PMC-360Si-3-28E-1000 fiber for incoupling
- Schäfter+Kirchoff 60FC-4-A7.5-01 input collimator
- $6 \times$ Schäfter+Kirchoff 60FC-4-M8-33 output collimators
- $6 \times$ OPM-11-405-3/125-P-3A3A-1-0.8-4-SI-TO18 OZ Optics fibers for outcoupling

Note that it is acceptable to use type M collimators at the output as the power at each of the outputs is low compared to that at the input.

The setup after assembly is shown in Fig.(4.2). A coupling efficiency of $\approx 50 - 51\%$ is achieved at each of the six output collimators. The power going to each of the output collimators can be controlled by turning the half waveplates accordingly until the desired power is achieved.

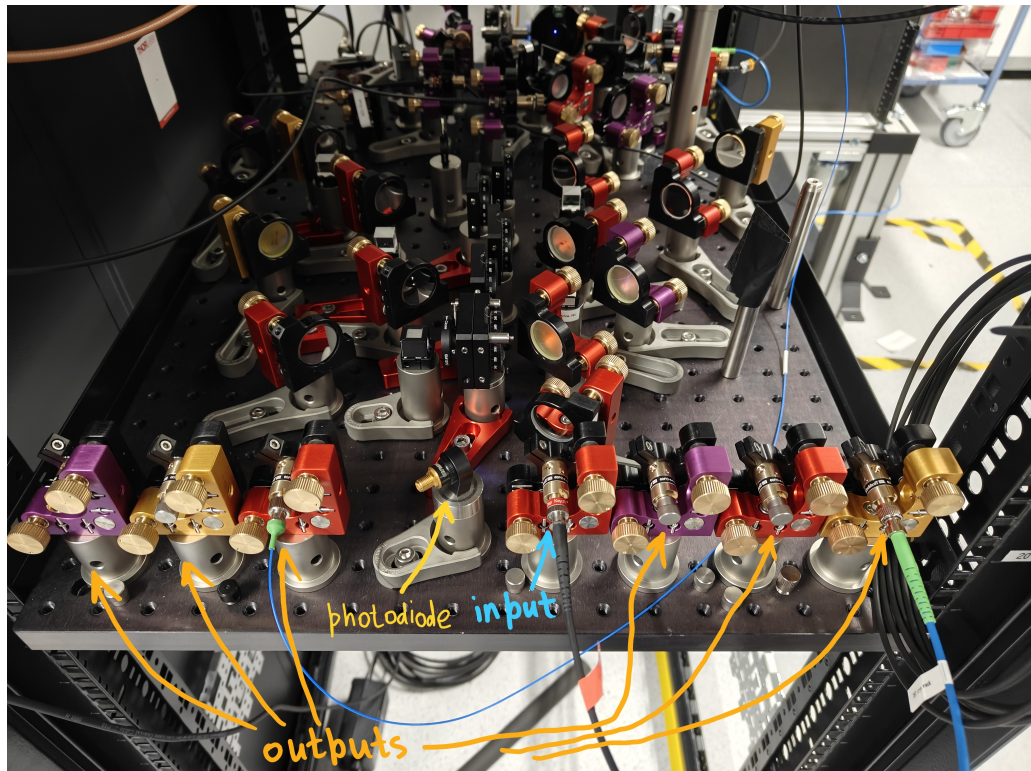


FIGURE 4.2: A picture of the splitting board after assembly.

Chapter 5

Conclusion

Scope for Improvement

The following possibilities may be explored further to improve the setup:

- The controller implementation of the SINARA may be improved by further analysis of the dual-iir source code, for example, by using a smaller batch size as discussed in Section(3.3). Alternately, other hardware with lower latency could also be considered.
- For long-term experiments, the RF source may be replaced with alternatives such as the SINARA Urukul, since the Moku:Pro is primarily intended for testing and probing.
- It was observed that the beam diameter at the input of the power stabilization AOM was relatively large, exceeding a millimeter, which resulted in inefficient diffraction of light into fringes other than the zeroth order fringe. A beam diameter close to 0.25 mm is considered optimal for the Gooch & Housego 3200-1210 AOM [26]. This could be addressed by appropriately inserting lenses in the beam path before and after the AOM. However, due to spatial constraints on the pre-machined optical board, this was not feasible without modifications.
- The splitting board may be miniaturized into a custom machined board with smaller optical components that would occupy less space.

Summary

A beam delivery setup for the 397 nm laser was designed and assembled. Intensity stabilization of the laser was achieved by implementing a PI controller using the SINARA Stabilizer, which provides a noise rejection bandwidth of 40 kHz . The bandwidth was found to be limited by the relatively large delay of the SINARA, measured to be $25\mu s$ which is unsuitable for pulsed applications that require delays of less than one microsecond. The laser intensity after stabilization had fluctuations of $\approx 0.4 - 0.6\%$ compared to $5 - 6\%$ of the unstable raw laser. Furthermore, a 1-to-6 splitting board was also assembled. A coupling efficiency of $\approx 50\%$ was achieved for each of the output collimators of the splitting board.

Bibliography

- [1] S. Seidelin, J. Chiaverini, R. Reichle, J. J. Bollinger, D. Leibfried, J. Britton, J. H. Wesenberg, R. B. Blakestad, R. J. Epstein, D. B. Hume, W. M. Itano, J. D. Jost, C. Langer, R. Ozeri, N. Shiga, and D. J. Wineland, “Microfabricated surface-electrode ion trap for scalable quantum information processing,” *Phys. Rev. Lett.*, vol. 96, p. 253003, Jun 2006.
- [2] J. Thom, B. Yuen, G. Wilpers, E. Riis, and A. G. Sinclair, “Intensity stabilisation of optical pulse sequences for coherent control of laser-driven qubits,” *Appl. Phys. B*, vol. 124, May 2018.
- [3] C. Mordini, A. Ricci Vasquez, Y. Motohashi, M. Müller, M. Malinowski, C. Zhang, K. K. Mehta, D. Kienzler, and J. P. Home, “Multizone trapped-ion qubit control in an integrated photonics qcccd device,” *Physical Review X*, vol. 15, no. 1, p. 011040, 2025.
- [4] J. Kwon, W. J. Setzer, M. Gehl, N. Karl, J. Van Der Wall, R. Law, M. G. Blain, D. Stick, and H. J. McGuinness, “Multi-site integrated optical addressing of trapped ions,” *Nature communications*, vol. 15, no. 1, p. 3709, 2024.
- [5] K. K. Mehta, C. Zhang, M. Malinowski, T.-L. Nguyen, M. Stadler, and J. P. Home, “Integrated optical multi-ion quantum logic,” *Nature*, vol. 586, no. 7830, pp. 533–537, 2020.
- [6] J. Eschner, G. Morigi, F. Schmidt-Kaler, and R. Blatt, “Laser cooling of trapped ions,” *J. Opt. Soc. Am. B*, vol. 20, pp. 1003–1015, May 2003.
- [7] D. Nadlinger, *Laser intensity stabilization and pulse shaping for trapped-ion experiments using acousto-optic modulators*. PhD thesis, Thesis, 2013.
- [8] “<https://www.dkphotonics.com/product/850nm-1x4-1x8-pm-fiber-splitter-module-1xn.html>,” *DK Photonics*.

- [9] “https://www.thorlabs.com/newgroupage9.cfm?objectgroup_id=12584pn=pn670r5a2,” *Thorlabs*.
- [10] C. F. Roos, “Ion trap quantum gates with amplitude-modulated laser beams,” *New Journal of Physics*, vol. 10, p. 013002, jan 2008.
- [11] “<https://www.doitpoms.ac.uk/tplib/photoelasticity/aims.php>,” *University of Cambridge DoITPoMS*.
- [12] C. D. Tran, “Acousto-optic devices,” *Analytical chemistry*, vol. 64, no. 20, pp. 971A–981A, 1992.
- [13] J. Eddie H. Young and S.-K. Yao, “Design considerations for acousto-optic devices,” *Proceedings of the IEEE*, vol. 69, no. 1, pp. 54–64, 1981.
- [14] B. Friedland, *Control system design: an introduction to state-space methods*. Courier Corporation, 2012.
- [15] D. Rowell, “State-space representation of lti systems,” URL: <http://web.mit.edu/2.14/www/Handouts/StateSpace.pdf>, pp. 1–18, 2002.
- [16] K. Ogata, “Modern control engineering,” 2020.
- [17] Z. Instruments, “Principles of pid controllers,” *Zurich Instruments: Zürich, Switzerland*, 2023.
- [18] A. Scottedward Hodel and C. Hall, “Variable-structure pid control to prevent integrator windup,” *IEEE Transactions on Industrial Electronics*, vol. 48, no. 2, pp. 442–451, 2001.
- [19] “<https://github.com/airwoodix/sinara-stabilizer-notes?tab=readme-ov-file>,” *sinara-stabilizer-notes*.
- [20] “https://hackmd.io/iacbwctst6adj3_f9bkuwpid-iir-primer,” *PID-IIR-Primer*.
- [21] D. R. Leibrandt and J. Heidecker, “An open source digital servo for amo physics experiments,” 2015.
- [22] “https://quartiq.de/stabilizer/firmware/src/dual_iir/dual-iir.rs.html#1-559,” *Batch size-SINARA*.
- [23] “<https://www.sukhamburg.com/support/technotes/fiberoptics/cablebasics/NAefftypvalues.html>,” *Schäfter + Kirchhoff*.

-
- [24] “<https://www.sukhamburg.com/support/technotes/fiberoptics/cablebasics/endcap.html>,” *Schäfter + Kirchhoff*.
 - [25] “<https://www.sukhamburg.com/support/technotes/fiberoptics/coupling/couplingbasics/lenstypes.html>,” *Lens types: Schäfter + Kirchhoff*.
 - [26] “https://www.eqphotonics.de/wp-content/uploads/gh_aom_3200-1210_97-02377-01.pdf,” *Gooch & Housego*.